Developments in the Built Environment 6 (2021) 100044

Contents lists available at ScienceDirect

Developments in the Built Environment

journal homepage: www.editorialmanager.com/dibe/default.aspx

Self-healing potential of supplementary cementitious materials in cement mortars: Sorptivity and pore structure

Riccardo Maddalena [a,*], Hussameldin Taha [b], Diane Gardner [a]

[a] Cardiff University, School of Engineering, Cardiff, CF24 3AA, UK
[b] University of Bath, Department of Architecture & Civil Engineering, Bath, BA2 7AY, UK

ARTICLE INFO

Keywords:
Autogenous healing
Mortar
Sorptivity
Cement replacement

ABSTRACT

This paper presents the autogenic self-healing potential of Portland cement (PC) blends made with conventional supplementary cementitious materials (SCMs), to improve the water-tightness by reducing the overall pore size. Mortar samples were prepared by mixing PC, sand and water, and partially replacing PC by either silica fume (SF), pulverised fuel ash (PFA), or ground granulated blast-furnace slag (GGBS). Damaged samples were subjected to a water bath to heal microcracks and recover the water-tightness, by further hydration of the starting minerals. Water absorption and density measurements in undamaged, damaged and healed conditions were used to determine the autogenous healing potential of SCMs mixes, showing a post-healing absorption recovery of up to 68% compared to the mix with PC only. Thermal analysis, XRD and MIP measurements confirmed the capability of SCMs to promote the formation of hydrated phases, and reduce the overall pore size by more than 88% compared to PC mixes.

1. Introduction

Cracking, weathering and carbonation are but a few examples of the main causes of damage in concrete (Gardner et al., 1016). Cracks that appear on the surface are often a precursor to deterioration as they facilitate water ingress and the transportation of harmful agents (e.g. chloride). This, in turn, may trigger reinforcement depassivation which leads to reinforcement corrosion (Angst et al., 2009). Alternatively, when salts and water penetrate the pores, the pressure exerted during the salt crystallisation may cause damage to the concrete structure (Espinosa--Marzal et al., 2011). Whilst modern construction design practices take into account possible scenarios to minimise damages and increase the service life of concrete structures, their maintenance still represents an economical and environmental burden. It is estimated that in the USA $33 billion alone is needed to repair the existing road bridges network (Treacy et al., 2019), while in the UK £6 billion has budgeted for 2015 to 2021 (Balogun et al., 2019). Researchers have studied and developed technologies to provide crack-closure mechanisms without external intervention. So-called self-healing concrete provides a solution to repair cracks at different temporal and spatial scales, and can potentially reduce an asset's maintenance costs (Huang et al., 2016; De Belie et al., 2018; Sidiq et al., 2020).

Various techniques based on autogenic (natural) or autonomic (engineered) healing have evolved over the last two decades. An advantage of the latter is that it has the potential to provide a self-healing effect within a very short timescale. Researchers have examined autonomic methods for healing damage such as the manufacture and inclusion of flow networks filled with liquid healing agents (i.e. cyanoacrylates, epoxies) within cement and concrete specimens (Gardner et al., 2017; De Nardi et al., 1306; Li et al., 2020). Cracks can also be mechanically closed by using shape memory polymers tendons and fibres, as explored in laboratory and field trials (Teall et al., 2018; Maddalena et al., 2020). This brings the crack faces close enough together to facilitate autogenic healing. The inclusion of bacteria and nutrients in cement paste has proven to promote the healing of cracked mortar and concrete (Wang et al., 2014; Tziviloglou et al., 1016; Tan et al., 2020). Through the cracks, water penetrates the cementitious matrix, triggering the microbial activity. This results in the precipitation of calcium carbonate within the cracks, and subsequently self-healing. Conversely, autogenic healing benefits from greater compatibility of the healing products with the cementitious matrix, albeit at the expense of a short healing duration. For example, microcracks could be sealed by crystalline admixtures, superabsorbent polymers (SAPs), and liquid or powder-based autogenic healing agents stored within macro and

* Corresponding author.
E-mail address: MaddalenaR@cardiff.ac.uk (R. Maddalena).

https://doi.org/10.1016/j.dibe.2021.100044
Received 19 June 2020; Received in revised form 14 January 2021; Accepted 18 January 2021
Available online 1 February 2021

Table 1
Characteristics of starting materials: ordinary Portland cement (CEM I), silica sand (S), silica fume (SF), pulverised fuel ash (PFA) and ground granulated blast-furnace slag (GGBS).

Components	CEM I	Sand (< 2 mm)	SF	PFA	GGBS
	%	%	%	%	%
Clinker	96	–			
Gypsum added	4.00	–			
Chemical composition					
SiO_2	20.12	99.9	85.0	49.3	36.79
Al_2O_3	5.03	Traces		24.1	11.51
Fe_2O_3	3.12	Traces		9.7	0.42
CaO	64.53	–		6.8	39.24
MgO	3.34	–		1.1	8.1
SO_3	0.98	–	<2	3.3	1.03
Na_2O	0.16	–		1.2	0.37
Density (kg/m^3)	1400	2500	500–700	1000	1200
Specific gravity	3.10–3.30	2.50–2.60	2.20–2.30	2.40–2.50	2.80–2.90
Specific Surface Area (m^2/kg)	350–450		(15–20) × 10^3	300–600	350–550

microcapsules that are added into the fresh paste (Snoeck and De Belie, 2016; Snoeck et al., 1016; Ferrara et al., 2018; Cuenca et al., 1016; Van Mullem et al., 2020). Due to their high specific surface area, plastic fibres (e.g. polyvinyl alcohol, polypropylene, etc) have also been studied in self-healing concrete (Nishiwaki et al., 2014; Rajczakowska et al., 1220). Researchers demonstrated that plastic and steel fibres not only contribute to bridging microcracks, but also act as nucleation sites for the formation of hydrated products, resulting in crack-healing. Specifically, fibre-reinforced concrete and engineered cementitious composites have been proposed as a viable solution to stimulate autogenous healing and provide crack closure of crack-widths up to 0.3 mm (Ferrara et al., 2017; Cuenca and Ferrara, 2017; Liu et al., 2017a).

Supplementary cementitious materials (SCM) are primarily industrial by-products or waste (e.g. steel industry, coal extraction, etc.). Their amorphousness and high pozzolanic reactivity promote the formation of hydrated products, such as calcium silicate hydrate (C–S–H) (Lothenbach et al., 2011; Berodier and Scrivener, 2014). SCMs have been proven to control fresh paste properties, such as bleeding and workability, and enhance the overall mechanical properties and durability of the cement paste in its hardened state when compared to mixes made entirely with Portland cement (Wainwright and Rey, 2000). It has also been demonstrated that SCMs play an important role in reducing the overall porosity of hydrated Portland cement (Sahmaran et al., 2013; Leung et al., 2016; Almeida and Klemm, 2018; Yildirim et al., 2018; Saha, 2018). When mixed with Portland cement silica fume (SF), pulverised fuel ash (PFA) and ground granulated blast-furnace slag (GGBS) impact the overall hydration kinetics by delaying the first peak of hydration and achieving an increased long-term degree of hydration (Monteagudo et al., 2014). This will ultimately result in a higher concentration of unreacted minerals at 28 days when compared to ordinary Portland cement mixes (Van Tittelboom et al., 2012). When cracks occur water penetrates the matrix, triggering the formation of additional calcium silicate hydrate within the crack plane and available pores, along with the precipitation of calcite (Danner et al., Geiker). While self-healing technologies, such as super-absorbent polymers (SAPs), shape memory polymers (SMP), bacteria-based self-healing, encapsulated healing agents (macro and microcapsules), engineered fibres, provide crack closure for crack widths even greater than 0.15 mm (Huang et al., 2016), SCMs contribute to the process known as autogenic healing (Van Tittelboom et al., 2012; Snoeck and De Belie, 2016; Wang et al., 2019), by sealing smaller cracks (crack width < 0.15 mm). The inclusion of SCMs as a partial replacement of Portland cement in the construction industry is regulated by international standards, and their undoubtedly positive environmental impact is well documented (Salas et al., 2016; Sakir et al., 1209).

The manufacture of Portland cement is one of the largest contributors to anthropogenic CO_2 emissions (Kajaste and Hurme, 2016; Maddalena et al., 2018). Employing alternative materials, such as waste and by-products (e.g. SCMs with pozzolanic reactivity) as a partial replacement of Portland cement, has a positive environmental impact in the construction industry (Habert and Roussel, 2009; Kim et al., 2013). In addition, to address the United Nations (UN) Sustainable Development Goals (SDGs) (United Nations, 2019), using SCMs in combination with other self-healing technologies could contribute to reducing the need for maintenance, which in turn further reduces the use of Portland cement. This would result in a significant cut in CO_2 emissions (UN SD Goal 13), responsible consumption of raw materials and waste management (UN SD Goal 12), and a sustainable response to the increasingly urbanised environment (UN SD Goal 11).

The aim of the work presented in this paper was to assess the autogenous healing capability of conventional SCMs (SF, PFA, GGBS), in order to explore the potential for SCM mix design with an enhanced self-healing capacity. Such a mix could then be combined with other autonomic healing technologies to maximise the overall potential for crack-healing. Whilst cement mortar is widely employed in external rendering and masonry construction, in this work it has been chosen as a simplified system than concrete, to isolate and better highlight the autogenous healing mechanism provided by SCMs. A series of Portland cement/SCM mortar mixes were cast, cured, damaged and subsequently healed. The hydration characteristics (nature and quantity of hydration products) of the specimens in the undamaged, damaged and healed conditions were determined via microstructure characterisation analysis, powder X-Ray diffraction (XRD) and thermal analysis (TG/DSC). In addition, the overall porosity reduction and the recovery of water-tightness of the cement matrix, were used as successful measures of self-healing potential.

Table 2
Series and mix proportions of cement (CEM I) replacement (%, by mass) using silica fume (SF), pulverised fuel ash (PFA) or ground granulated blast-furnace slag (GGBS).

Series	CEM I	SF	PFA	GGBS
	%	%	%	%
C	100	–	–	–
S	90	10	–	–
P	70	–	30	–
B	50	–	–	50

2. Materials and methods

Mortar paste specimens were prepared using ordinary Portland cement CEM I (strength class 52.5 MPa), silica sand (particle size < 2 mm), at sand to binder (s/b) ratio of 3, and deionised water at water to binder (w/b) ratio of 0.45 (BS-EN 196-1:2016). All ratios were by mass. Portland cement (from CEMEX UK) was partially replaced by three SCMs at different percentages. Commercially available SCMs were used; silica

fume (SF), produced by Elkem Micro Silica, Norway; pulverised fuel ash (PFA), and ground granulated blast-furnace slag (GGBS), supplied by CEMEX UK. Four series of mixes were produced; a control mix with 100% of CEM I (C), a mix with 10% replacement of silica fume (S), a mix with 30% replacement of PFA (P) and a mix with 50% replacement of GGBS (B). Characteristics of starting materials are reported in Table 1. Series designation and replacement proportions by mass are reported in Table 2. The highest SCMs replacement levels allowed by the BS–EN 197–1:2011 (BS EN 197-1:2011. Composition, specifications and conformity criteria for common cements, 2011) were adopted in this work.

Mortar was prepared following BS–EN 196–1:2016 (BS EN 196-1:2016, 2016) and cast into brass moulds of 25 × 25 × 25 mm. After 24 h, specimens were demoulded and cured for 28 days in a closed container at controlled environmental conditions (95% relative humidity and 20 ˚C) to minimise carbonation (Cerveny et al., 2011).

The specimens' size and geometry (cube, 25 × 25 × 25 mm) was chosen to minimise the amount of time the sample is in contact with water during the tests to avoid swelling and microstructural changes (Alderete et al., 2019), and guarantee that the water absorbed by the specimens during the sorptivity and porosity measurements could be removed at a relatively high drying rate, in order to prevent further hydration and compromise the overall results (Chari et al., 2016; Benli and Bakir, 2017; Mora et al., 2019).

A total of 36 cubes were cast for each series. After curing, the samples were gently oven-dried at 55 ˚C for up to 5 days, until the change in weight recorded over a period of 3 h is less than 0.2% (Gallé, 2001).

Samples were damaged mechanically using a loading cell at a displacement ratio of 0.01 mm/s. For each series, three samples were subjected to compressive load until failure, to establish the maximum peak load. This value was then used to guide the level of load to apply to the remaining cubes to damage them to 90% of the peak load, in order to generate small microcracking within the specimens. The damaged cubes were then placed in a static healing bath of deionised water to promote further hydration and crack-healing for 60 days.

Physical characteristics and water transport properties (sorptivity) were measured on the four samples for each series in undamaged (u) conditions (after curing for 28 days), damaged (d) conditions (after mechanical loading external damage), and healed (h) conditions (after 60 days in deionised water). The mineral composition of the samples was determined in the damaged (d) and healed (h) conditions. The test procedures are summarised in the following sub-sections.

Sorptivity: The water absorption (also called sorptivity) test measures the water uptake rate through the capillary rise effect in the pore structure within a period of time. The measurement was used to determine the healing potential of the different SCM mixes. For each series, a minimum of three samples were used. The specimens were oven-dried at 55 ˚C for up to 5 days, until the change in weight recorded over a period of 3 h is less than 0.2%. This temperature was chosen to minimise C–S–H swelling and pore structure alteration that could impact the overall water capillary absorption (Gallé, 2001; Villagrán Zaccardi et al., 2017; Alderete et al., 2019). The specimens were then placed in a sealed container with 1 mm of their bottom surface in contact with deionised water. The water absorption rate was measured indirectly through the sample weight increase with time, over a period of 100 min at defined intervals (1, 4, 9, 16, 25, 36, 49, 64, 81, 100 min). The methodology was adapted from the ASTM C1585:2004 test method (ASTM and ASTM C 1585, 2004) and successfully trialled on small samples prior to the current study to establish the accuracy and efficacy of the approach adopted.

Open porosity and density: The test method proposed by the inter-laboratory comparison of hygric properties of porous building materials (HAMSTAD) (Roels et al., 2004) was followed to perform open porosity measurements, bulk density and matrix density on three specimens for each series at each stage; (u), (d) and (h).

X-ray diffraction and thermogravimetric analysis: Specimens for XRD and thermal analysis were broken into smaller pieces. The inner part of the specimen was crushed and powdered into homogenous particle sizes.

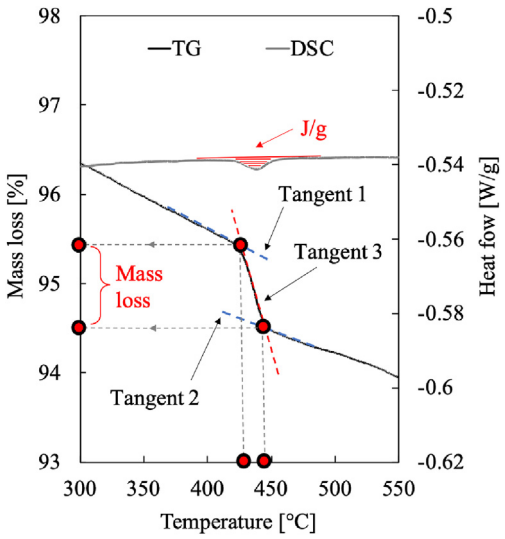

Fig. 1. Determination of TG mass loss and DSC response using the tangential method (Lothenbach et al., 2015).

The powder was further oven-dried at 55 ˚C for 5 days. XRD analysis was performed on a diffractometer (PANalytical X'ert Pro) using a Ni-filtered CuKα radiation source operating at 40 KV and 40 mA. Diffraction patterns were recorded between 5 and 80˚ 2θ at a step size of 0.0167˚ 2θ (resulting in a total run time of 40 min) using a back filled sample holder. Diffraction patterns were identified using the International Centre for Diffraction Data (ICCD) Powder Diffraction File (Faber and Fawcett, 2002). Thermal analyses were used to identify those mineral phases most likely to play a role in the healing process. Thermogravimetric (TG) and differential scanning calorimetry (DSC) curves were collected from 25 ˚C to 1000 ˚C at a heating rate of 10 ˚C/min under constant nitrogen flow, using a TGA/DSC 3+ thermogravimetric analyser (Mettler Toledo). A constant temperature of 60 ˚C was held for 10 min to stabilise the sample. A powder sample size of 20 ± 0.1 mg was used. Three measurements were collected for each series. The mass loss was calculated using the tangential method (Lothenbach et al., 2015). A detail of the tangents construction for the TG curve and for the DSC curve is given in Fig. 1. The mass loss in the TG signal, obtained from the intersection of the different tangents, was calculated at three different temperature ranges; 90–150 ˚C, temperature range of pore-water evaporation, and the decomposition of both C–S–H and ettringite; 440–440 ˚C, dehydroxilation of portlandite; and 660–700 ˚C, decomposition of carbonated products (Maddalena et al., 2019). TG mass loss at the specific temperature range was used to estimate the mineral phase relative content in damaged (d), and healed samples (h).

Mercury Intrusion Porosimetry (MIP): MIP (Thermo Scientific, Pascal 140/440), was used for pore size distribution measurements and total porosity calculation analysis of samples in damaged (d) and healed (h) conditions. A 2 mm thick slice was cut from the centre of each cube, oven dried at 55 ˚C for 5 days and subjected to vacuum drying for 24 h, to remove all water from the pores. The specimen was then introduced into a glassy dilatometer for MIP measurements. In the MIP device, a degassing process took place by applying a vacuum pressure as a pre-conditioning stage; then the dilatometer was filled with mercury, and an increasing pressure was applied. The maximum mercury pressure applied was 400 MPa, which allowed access to pores of the order of 2 nm in diameter, assuming a 140˚ mercury contact angle according to the Washburn equation (Koniorczyk et al., 2013). The measurement was repeated on three different slices of one sample for each series and the pore diameters were given as a mean value.

The healing mechanism investigated in this work relies on the key role played by SCMs and their hydration kinetics in promoting further formation (over time) of additional hydrated products in presence of

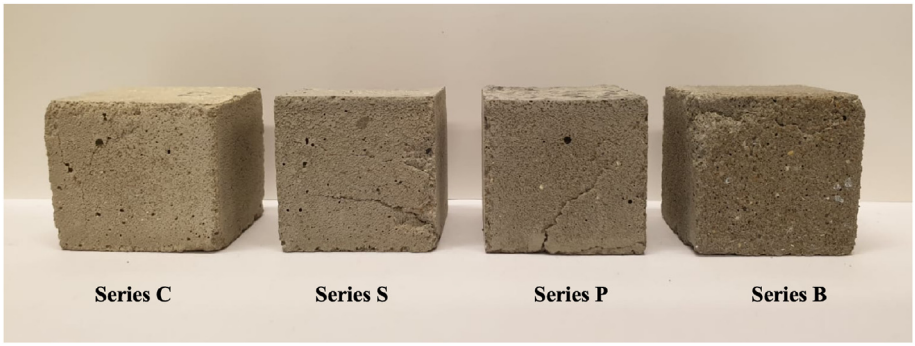

Fig. 2. External damage of representative samples after mechanical loading.

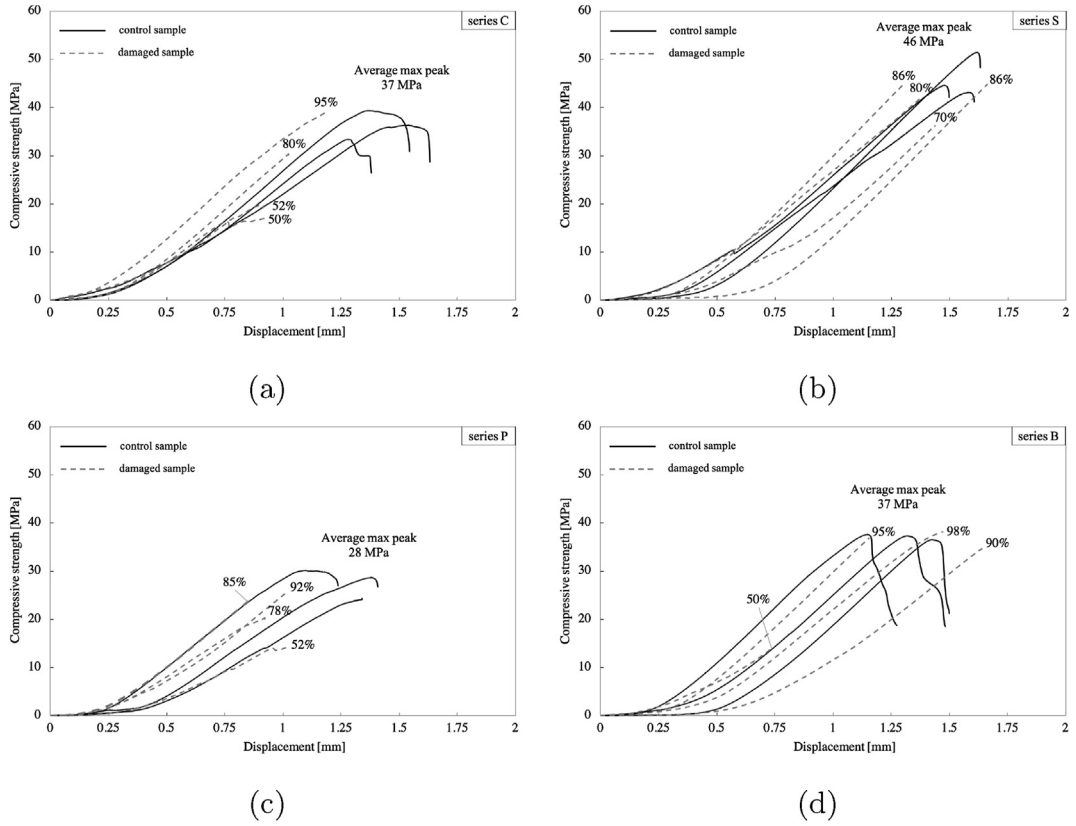

Fig. 3. Reduced mechanical loading of the samples (dashed grey lines); Portland cement series C (a) silica fume series S (b), PFA series P (c) and GGBS series B (d) compared with the ultimate mechanical loading of the control samples for each series (black lines).

water (healing bath). The healing process, which takes place at the microscale level, results in a densification of the microstructure and a complex pore structure evolution over time. Thus the self-healing ability of SCM mixes will be described as the relative change in hydrated phases and pore structure between initial (undamaged) and final (healed) conditions of the same specimens, and compared to the Portland cement mortar series. It must be noted that sorptivity (as well as porosity, thermogravimetric, and mineralogical) values were determined from the same specimens at the different stages (undamaged, damaged and healed), as oppose to a direct comparison to an undisturbed reference (or control) series.

3. Results and discussion

Cube specimens were mechanically loaded to a target load of 90% of their maximum peak load, this resulted in varying degrees of external damage, as observed on the surfaces of the test specimens (Fig. 2). The associated load–displacement responses for the various specimens are presented in Fig. 3, where the original peak load for each series (C, S, P and B) is reported in black and the reduced 90% target load is given in dashed grey. Difficulties in conducting the test on the small specimens resulted in damage loads between 50 and 98% being observed in the test. The average values of compressive strength recorded for all the four series was in the range of 28–46 MPa. Although the values obtained might not reflect the real compressive strength of the mixes, i.e. the sample size differs from the dimension recommended by the BS EN 196–1:2016, however, said values are a good estimation of the strength, in agreement with literature values for cement mortars incorporating SCMs (Benli and Bakir, 2017; Monteagudo et al., 2014; Almeida and Klemm, 2018). A number of samples in series C, P, and B presented visible damage (cracks or fracture) on the surface at low percentage of loading (approximately 50%), and any further increase in load would have resulted in the sample

Table 3
Average values (CoV < 5%) of open porosity (φ), bulk density (ρ), matrix density (ρ_{mat}), the cumulative water absorption at 25 min (I_5, 5 $min^{0.5}$), and the total absorption at 100 min from the beginning of the sorptivity test (I_{10}, 10 $min^{0.5}$) in undamaged (u), damaged (d) and healed (h) conditions.

Series		φ	ρ	ρ_{mat}	I_5	I_{10}
		%	g/cm^3	g/cm^3	mm	mm
	(u)	18	2.05	2.49	3.1	4.2
C	(d)	18	2.03	2.47	3.7	4.1
	(h)	19	2.03	2.51	1.9	3.3
	(u)	17	2.02	2.44	2.6	4
S	(d)	18	2.01	2.43	2.6	3.7
	(h)	19	2.00	2.46	0.9	2
	(u)	18	2.01	2.46	4.0	4.1
P	(d)	18	2.00	2.46	3.9	4
	(h)	19	2.01	2.48	1.9	2.9
	(u)	19	2.01	2.49	4.3	4.5
B	(d)	19	2.02	2.49	4.0	4.3
	(h)	20	2.02	2.51	1.7	2.9

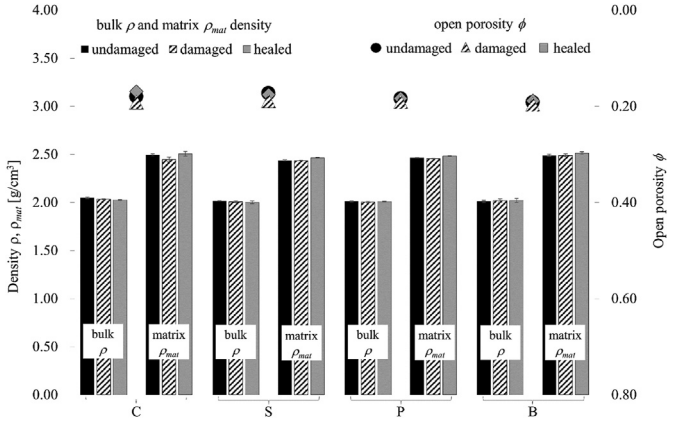

Fig. 4. Average values (CoV < 5%) of bulk (ρ) and matrix density (ρ_{mat}), and open porosity (φ), in undamaged (u), damaged (d) and healed (h) conditions.

failure, hence loading was terminated at this point.

The results from density, porosity and water absorption measurements of the different series in undamaged (u), damaged (d) and healed (h) conditions are reported in Table 3 and Fig. 4. The values obtained are typical of mortar-based cementitious materials with an acceptable statistical variation (coefficient of variation, CoV < 5%) (Hall and Hall, 1989). While the bulk density values (ρ) do not show significant change between undamaged (u), damaged (d) and healed (h) conditions, the matrix density (ρ_{mat}) increases after the healing stage by 0.44%, 1.13%, 0.71% and 0.97% for series C, S, P and B respectively. It suggests that the overall specific weight of the samples has increased due to the formation of additional hydration products within the structure. The open porosity (φ) values are almost constant throughout the three stages (u), (d) and (h). It should be noted, however, that the methodology for the measurement of open porosity (φ) provides an estimate of the accessible open pores' volume, and might not be suitable to detect any pore clogging at the microscale induced by autogenous healing. The pore structure is explored using mercury intrusion porosimetry (MIP), as discussed later in this section.

The water absorption (I) curves for series S, P and B are reported in Fig. 5 and compared with the curves of series C. The values reported are the average of three measurements. Table 3 reports also the cumulative water absorption at 25 min (I_5, 5 $min^{0.5}$), and the total absorption at the end of the sorptivity test after 100 min (I_{10}, 10 $min^{0.5}$). Comparing undamaged (u) and healed (h) conditions, I_{10} decreased by approximately 21% in series C, and by 50%, 30% and 35% in series S, P and B, respectively.

The total water absorption I_{10} values at 100 min are typical of cement-

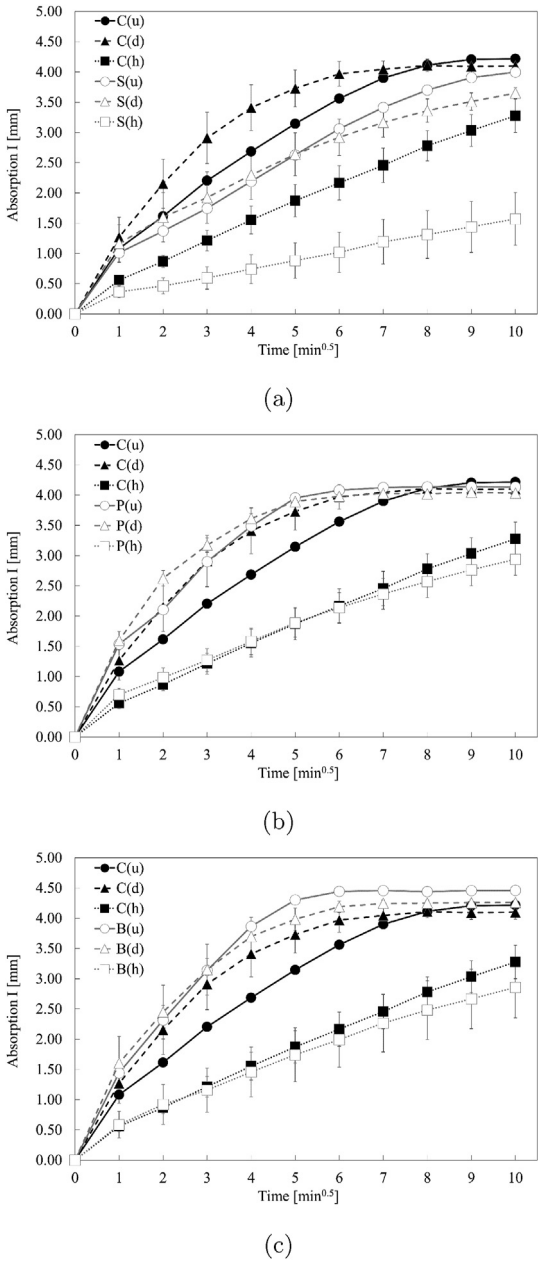

Fig. 5. Water absorption curves of (a) series S, (b) series P and (c) series B compared with the control series C, in undamaged (u), damaged (d) and healed (h) conditions.

based mortar (Hall and Hall, 1989; Ren et al., 2019) and similar for undamaged (u) and damaged (d) conditions; while this may be due to the size of the sample and the variability in mechanical damage induced by uniaxial loading, as reported in Fig. 3, or possibly due to a small loss of matrix which can absorb water, their response is different in the two cases, showing that the loading has caused significant changes in the microstructure, and subsequent rate of water absorption. At the early stages of the test and within the first 25 min (I_5, 5 $min^{0.5}$), the slope of the damaged samples is higher when compared to the undamaged series, as reported in Fig. 6. Whilst this is more evident in series C, it is however recorded in series S, P and B. In the latter, the water absorption at 4 and 5 $min^{0.5}$ is slightly lower for the damaged samples, as shown in Fig. 6d. This could be attributed to the variability of the mechanical tests, as shown in Fig. 3d, as well as the geometry, size of the sample or matrix loss, where the intrinsic heterogeneity of the cementitious system at this scale could induce a different degree of damage and scatter the result

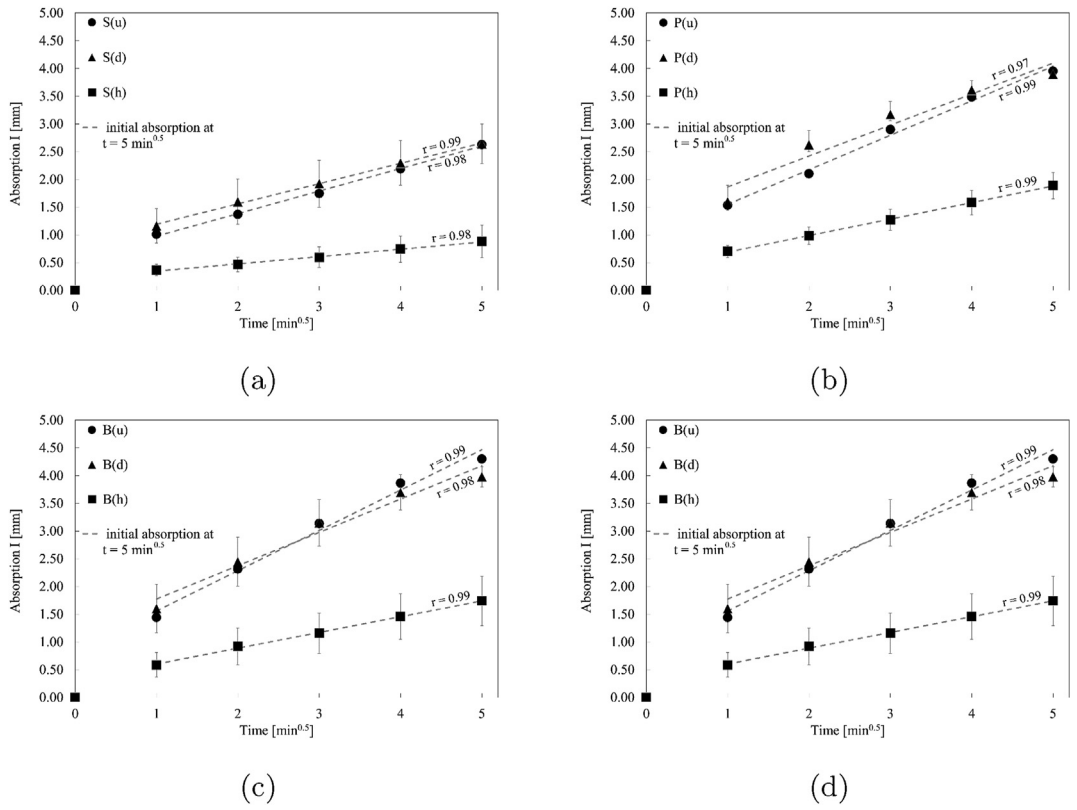

Fig. 6. Initial water absorption up to t = 5 min$^{0.5}$ of (a) series C, (b) series S, (c) series P and (d) series B, in undamaged (u), damaged (d) and healed (h) conditions, and calculated slope for each series. r is the correlation factor.

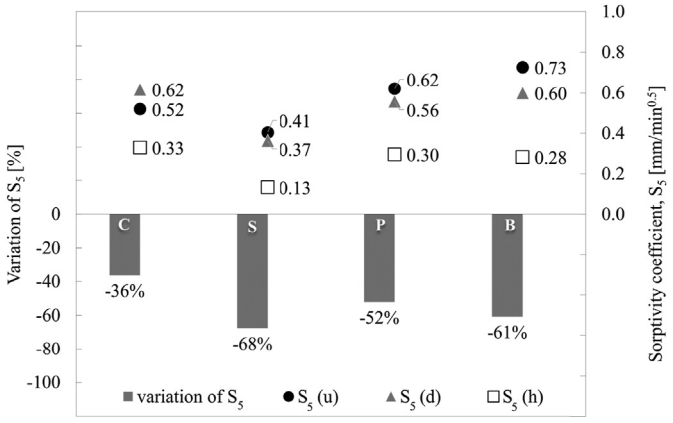

Fig. 7. Coefficient of sorptivity S_5 measured up to t = 5 min$^{0.5}$ for samples at undamaged (u), damaged (d) and healed (h) condition, and variation of S_5 comparing (u) and (h) conditions.

values, as indicated by the error bars. Finally, the reduced rate of water absorption in the healed samples, together with the reduction in total water absorption, provides evidence of crack- or pore-filling and sealing. This effect is more pronounced in the mixes containing SCMs than the control mix (Zhang et al., 2014; Leung et al., 2016). In undamaged (u) and damaged (d) conditions, distinct primary and secondary water absorption stages are apparent (Hall and Hamilton, 2018), where it takes only few minutes (approximately 25 min, t = 5 min$^{0.5}$) to reach a saturated state; on the contrary, in healed (h) conditions, the imbibition rate continues to increase beyond the initial 25 min. Fig. 7 shows the coefficient of water sorptivity S_5, as the slope of the initial part of the absorption curve, calculated at t = 5 min$^{0.5}$ (25 min), and its variation between undamaged (u) and healed (h) conditions. All the SCMs mixes exhibit a significant reduction in the S_5 between undamaged and healed conditions, with a total 68% reduction for series S and a maximum reduction of 36% for series C. Even prior to damage and healing, the silica fume particles (with a minimum replacement of 10% by mass) act as a filler, inhibiting the access of water to pores (Lothenbach et al., 2011; Quercia et al., 2012); thus series S shows an overall lower S_5 compared to the other series. Furthermore, silica fume particles provide a nucleation site for crystal formation, which consequently leads to additional precipitation of calcium silicate hydrate (C–S–H) (Hatungimana et al., 2019). Similarly, the series with PFA (P) and the series with GGBS (B) contributed to the reduction in initial sorptivity S_5 of 52% for the former and 61% for the latter when comparing the undamaged (u) to the healed (h) conditions. In the undamaged conditions, unreacted PFA and GGBS particles fill up the pore space, absorbing water at a higher rate than plain Portland cement mortar (C), as shown in Fig. 5b and Fig. 5c (Gopalan, 1996; Park and Choi, 2018). However, after a period of healing in water for two months, their S_5 showed a significant reduction. This is due to the further hydration of PFA and GGBS particles: Ca and Si ions from GGBS and PFA particles are dissolved under alkaline conditions and precipitate in pores and microcracks forming additional C-(A)-S-H phases (Liu et al., 2017b; Park and Choi, 2019).

XRD patterns of series S, P and B in damaged (d) and healed (h) conditions compared to series C are shown in Fig. 8. The peaks at ca. 18°, 34° and 47° 2θ are the reflection of $Ca(OH)_2$ (portlandite) crystals. Their reduced intensity for all the SCM mixes after healing suggests that the portlandite, naturally present in hydrated cement pastes, reacted with water during the healing stage, to form additional C–S–H. The patterns showed an increase in intensity of the peaks associated to C–S–H, at ca. 29°, 32°, 50°, 55° and 60° 2θ, confirming the observations above.

Normalised thermogravimetric (TG) and differential scanning calorimetry (DSC) representative curves of control series C at damaged (d) and healed (h) conditions are reported in Fig. 9. Downward peaks in the DSC curves indicate an endothermic reaction.

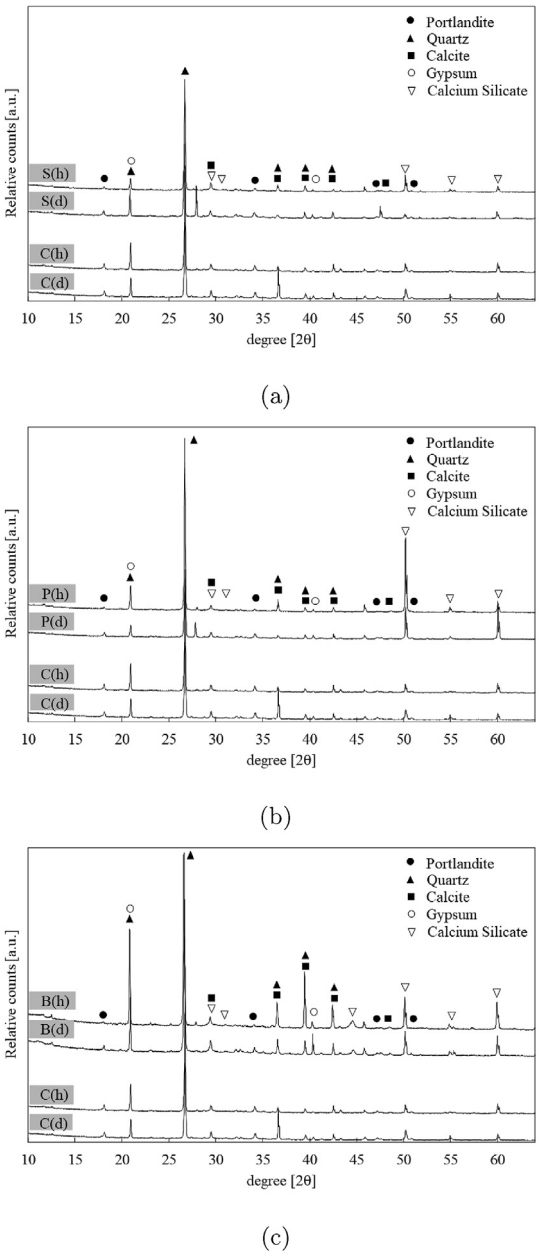

Fig. 8. XRD pattern of (a) series S, (b) series P and (c) series B compared with the control series C in damaged (d) and healed (h) conditions.

TG and DSC curves were obtained for the other SCM series, from which the relative mass loss change between damaged (d) and healed (h) conditions for all series (C, S, P and B) presented in Fig. 10 were determined. These are expressed in thermal steps of 90–150 ˚C, 410–440 ˚C, and 660–700 ˚C, typically associated with water loss and C–S–H dehydration, portlandite dehydroxylation, and calcite decomposition, respectively.

When compared to the damaged state, the healed series C shows a reduction in TG mass loss in the first and second thermal step (C–S–H, pore water and ettringite in the former and portlandite in the latter), counteracted by an increase in mass loss due to carbonated products. Series S, P and B show a significant reduction in TG mass loss of portlandite when comparing healed (h) to damaged (d) conditions, balanced by an increase in the TG mass response of C–S–H. This suggests that the calcium species available were consumed to form additional C–S–H (Danner et al., Geiker). Furthermore, the delayed hydration promoted by the presence of SCMs contributed to the formation of additional calcium

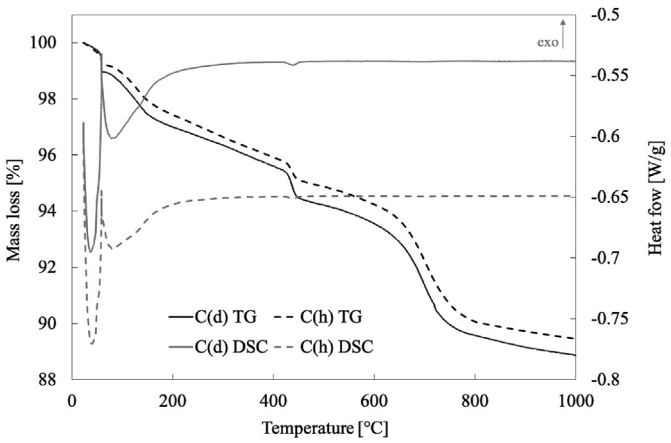

Fig. 9. TG curves of a representative sample for control mix (C), in damaged (d) and healed (h) conditions.

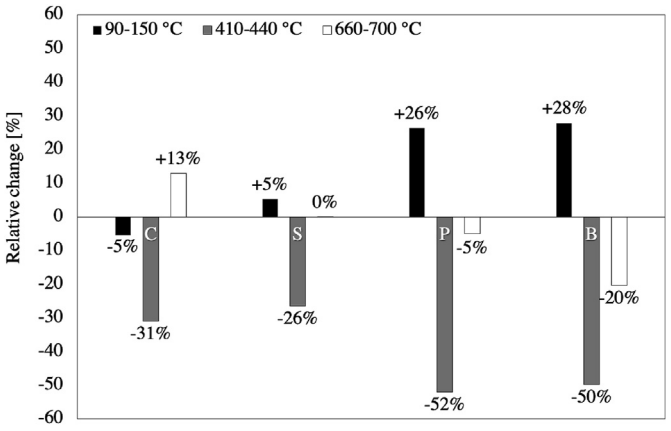

Fig. 10. Mass loss relative change (from damaged to healed conditions) calculated from TG responses at three different temperature ranges, 90–150 ˚C, 410–440 ˚C and 660–700 ˚C respectively.

(aluminum) silicate hydrate, C-(A)-S-H, during the healing process rather than the initial curing stage, reducing the amount of calcium species that would otherwise precipitated into calcite (Liu et al., 2017b; Almeida and Klemm, 2018). The higher initial content of CaO present in the starting GGBS resulted in the highest reduction of carbonated products (series B, 20%).

In the mix with a 10% replacement of silica fume (series S) an increased TG mass loss in the temperature range 90–150 ˚C was observed. Since this range is associated with the evaporation of pore water and dehydration of C–S–H, it could suggest a greater quantity of C–S–H (+5% in TG mass loss) in the sample S(h) after healing. The formation of C–S–H is possible because of the consumption of portlandite (−26% in TG mass loss). The additional formation of C–S–H during the healing stage is more evident in samples P and B and can be attributed to their chemical

Table 4
DSC response in the thermal range of portlandite (400–440 ˚C). Values reported are an average of 3 measurements, (CoV <15%).

Serie	DSC response 400–440 ˚C		Reduction
Mix	J/g	J/g	in $Ca(OH)_2$
	(d)	(h)	%
C	0.31	0.20	36
S	0.17	0.10	43
P	0.17	0.06	65
B	0.07	0.04	48

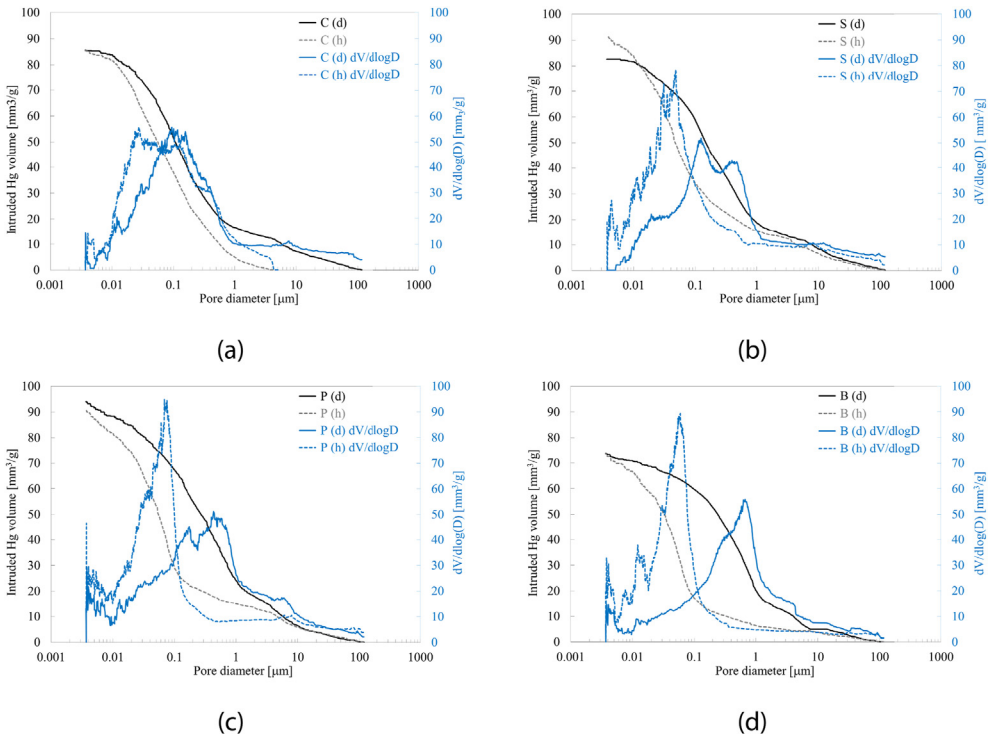

Fig. 11. Changes in pore size distribution of representative samples for the control series C (a), series S (b), series P (c) and series B (d) in damaged (d) and healed (h) conditions. [Cumulative pore volume in black, differential pore size in blue]. (For interpretation of the references to colour in this figure legend, the reader is referred to the Web version of this article.)

Table 5
Pore size diameter (d50) equivalent to the 50% of total intruded mercury volume, and porosity values obtained from MIP measurements. Values are calculated on an average of three measurements (CoV <20%).

Serie	Total porosity		d_50		Reduction
	%		nm		in pore size
	(d)	(h)	(d)	(h)	%
C	16.5	17.9	169	74	56
S	15.9	17.9	194[a]	56	71
P	19.9	18.9	373[a]	60	84
B	17.9	18.9	559	69	88

[a] average between the two peaks in the bimodal distribution.

composition and their high pozzolanic reactivity (Park and Choi, 2018). Increasing the Portland cement replacement from 10% to 30% and 50% respectively for series S, P and B, resulted in an increased TG mass loss in the first thermal step of 5%, 26% and 28% respectively.

The DSC response (i.e. the normalised integral) for the thermal step 400–440 ˚C associated to the dehydroxylation of portlandite was calculated for each series. The relative change between damaged (d) and healed (h) condition is reported in Table 4. All the mixes with SCMs have a higher reduction in the intensity and amplitude of the portlandite DSC signal compared to series (C). Similarly to the TG results, the DSC response of series (P) with 30% replacement of PFA showed the highest reduction in portlandite (65%) after healing.

To further explore the effect of different SCMs on the self-healing capability and the cement pore structure, mercury intrusion porosimetry (MIP) measurements were carried out on all the mixes in damaged (d) and healed (h) conditions. The cumulative intruded mercury volume (in mm^3/g) curves are reported in Fig. 11. The healing process was found to affect the pore size distribution in all series; with smaller pore diameters reported after healing for all intruded mercury volumes. However, this was more evident in the series with cement replacement

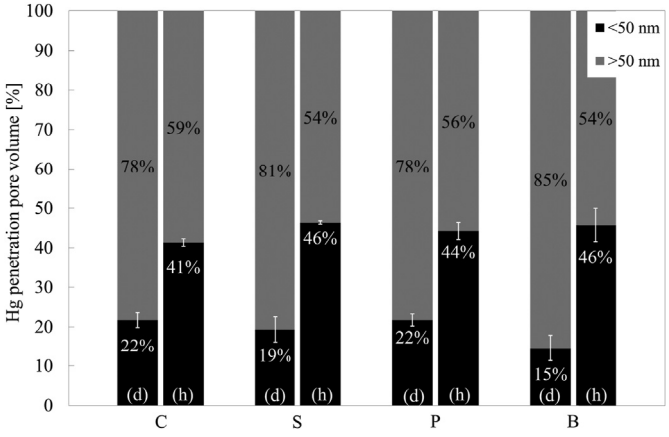

Fig. 12. Normalised volumes of micropore (<50 nm) of all mixes at damaged (d) and healed (h) conditions. Values reported are an average of 3 measurements (CoV <40%).

materials (Fig. 11b, c and Fig. 11d). Whilst series C and B exhibit a unimodal distribution before and after the healing process, two distinct peaks at approximately 100 nm and 300 nm for series S; and 170 nm and 500 nm for series B respectively, are visible at damaged conditions. A bimodal distribution suggests a complex pore structure due to the different mechanism of pore structure formation: capillary pores and gel pores (Zhang et al., 2019). However, at healed conditions, the pore size distribution appears to be unimodal, with peaks centred at 56 nm and 60 nm for series S and series P respectively, showing a uniform reduction in pore size.

The average pore diameter (d_50) values, equivalent to the 50% of the volume of mercury intruded, in damaged (d) and healed (h) samples are reported in Table 5. For series S and series P, the average value between the two peaks of the bimodal distribution is reported. While series C and

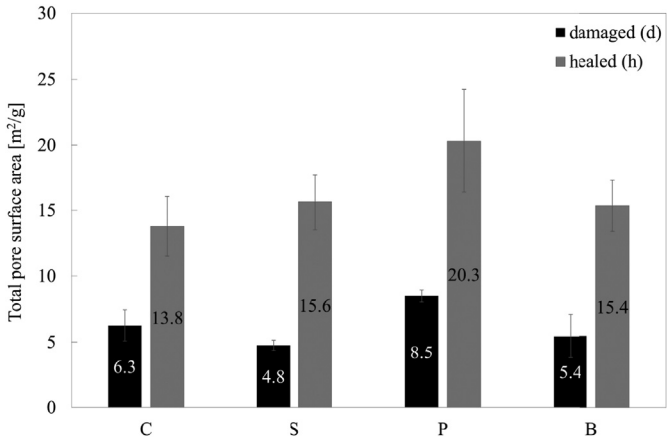

Fig. 13. Total pore surface area (in m^2/g) of all mixes at damaged (d) and healed (h) conditions. Values reported are an average of 3 measurements (CoV <30%).

S show an initial average pore diameter of 169 and 193 nm respectively, series P and B show a larger average diameter of 373 and 431 nm respectively. This can be attributed to the larger particle size of PFA and GGBS compared to Portland cement that could compromise the reactivity of the initial PFA and GGBS particles and delay the formation of hydrates (Lothenbach et al., 2011; Almeida and Klemm, 2018). However, after healing, the average d_50 value for series P and B decreases significantly to 60 and 69 nm, respectively. Similar results are found in literature, where mortar mixed with 40% replacement of GGBS exhibits a more refined pore structure at 90 days compared to the one at 28 days (Alderete et al., 2017). Fig. 12 shows the significant variation in pore size volumes. The percentage of pores in the micropore region (> 50 nm) doubles in series C, S and P, and triples in series B. As pores in diameter > 50 nm impact the water transport properties of hydrated cement, a counter-reduction in their volume improves the durability of the mix and its resistance against chemical attack, e.g. chloride penetration (Sahmaran et al., 2013). While the total porosity for the healed samples did not show a significant change from the damaged samples (reported in Table 5), the values of pore diameters (d_50) decreased significantly. This suggests that the healing process has a greater influence on the connected porosity rather than the total porosity through decreasing the size of the pores as well as disconnecting the continuous pores (Mehta and Monteiro, 2006; Sahmaran et al., 2013; Alderete et al., 2017).

The MIP results were also used to calculate the total pore surface area for samples in damaged (d) and healed (h) conditions. The average values (in m^2/g) are reported in Fig. 13. The surface area values in the damaged condition are typical of mortar concrete (Johannesson and Utgenannt, 2001; Anwar and Emarah, 2019). All series showed an increases in the pore surface area after healing. It has been shown in Fig. 10 that the healing process resulted in the formation of additional C–S–H and associated products of hydration, both within the pores and the microcrack surfaces (Van Tittelboom et al., 2012), increasing the amount of precipitated minerals and thus the overall pore surface area.

4. Conclusions

Crack formation is one of the main causes of deterioration in cement and concrete. Cracks in the cover zone lead to fluid ingress and subsequent modification of the pH of the cement matrix. This, in turn may result in disruption to the passive film that protects steel reinforcement, the onset of rust formation and the overall safety of a concrete element being compromised. This work investigated the self-healing capability of cement-based mortar mixes partially replaced by 10% of silica fume, 30% PFA, and 50% GGBS and compared with mortar made with 100% Portland cement. Samples were mechanically loaded to induce internal damage (in the form of microcracking), then placed in a water bath for two months to trigger further hydration and crack healing. It was found that the reactivity of supplementary cementitious materials (SCMs) samples promoted the formation of additional calcium silicate hydrate (C–S–H) which decreases their initial water absorption rate by 68% for mixtures including silica fume and 52% and 61% for samples mixed with PFA and GGBS respectively.

Thermal analysis showed that all the SCMs promoted self-healing processes by consuming calcium hydroxide (portlandite) to form additional C–S–H and in doing so minimise the potential for carbonation. Microstructural analysis revealed that, after healing, the overall pore size diameters decreased by up to 84% for samples containing PFA and GGBS, when compared to the ones mixed with Portland cement only (56%).

The results showed that each SCM promoted the autogenous healing through different mechanisms (pore filling action and deposition of additional minerals, continued hydration and pozzolanic action, as indicated by changes in the specific surface area and chemical composition), by the formation of additional hydrated products within the pores and the microstructure. This contributed to an overall decrease of water transport rate through the matrix and an improvement in pore size distribution.

This work showed that each of the SCMs investigated improves the self-healing capabilities and the overall porosity of all the series. Further work will investigate ternary replacement of Portland cement combining different percentages of silica fume, PFA and GGBS simultaneously, to further enhance the self-healing capability of cementitious materials, and improve the overall physical and chemical properties when combined with other self-healing technologies.

Declaration of competing interest

The authors declare that they have no known competing financial interests or personal relationships that could have appeared to influence the work reported in this paper.

Acknowledgement

This work is supported by UK Engineering and Physical Sciences Research Council (EPSRC), Grant No. EP/P02081X/1, Resilient Materials 4 Life, RM4L. Data associated with the research published and supporting information in this paper are accessible at http://doi.org/10.17035/d.2019.0088368190.

References

Alderete, N., Villagrán, Y., Mignon, A., Snoeck, D., De Belie, N., 2017. Pore structure description of mortars containing ground granulated blast-furnace slag by mercury intrusion porosimetry and dynamic vapour sorption. Construct. Build. Mater. 145, 157–165. https://doi.org/10.1016/j.conbuildmat.2017.03.245.

Alderete, N.M., Villagrán Zaccardi, Y.A., De Belie, N., 2019. Physical evidence of swelling as the cause of anomalous capillary water uptake by cementitious materials. Cement Concr. Res. 120 (April), 256–266. https://doi.org/10.1016/j.cemconres.2019.04.001.

Almeida, F.C., Klemm, A.J., 2018. Efficiency of internal curing by superabsorbent polymers (SAP) in PC-GGBS mortars. Cement Concr. Compos. 88, 41–51. https://doi.org/10.1016/j.cemconcomp.2018.01.002.

Angst, U., Elsener, B., Larsen, C.K., Vennesland, Ø., 2009. Critical chloride content in reinforced concrete – A review. Cement Concr. Res. 39 (12), 1122–1138. https://doi.org/10.1016/j.cemconres.2009.08.006.

Anwar, M., Emarah, D.A., 2019. Pore structure of concrete containing ternary cementitious blends. Results Mater. 1, 100019. https://doi.org/10.1016/j.rinma.2019.100019.

Astm, Astm C 1585, 2004. 2004 standard test method for measurement of rate of absorption of water by hydraulic-cement concretes. Tech. Rep.

Balogun, T.B., Tomor, A., Lamond, J., Gouda, H., Booth, C.A., 2019. Sustainability of bridge maintenance. Proc. Inst. Civ. Eng.: Bridge Eng. 172 (1), 54–64. https://doi.org/10.1680/jbren.15.00027.

Benli, A., Bakir, M. Karataş, 2017. An experimental study of different curing regimes on the mechanical properties and sorptivity of self-compacting mortars with fly ash and silica fume. Construct. Build. Mater. 144, 552–562. https://doi.org/10.1016/j.conbuildmat.2017.03.228.

Berodier, E., Scrivener, K., 2014. Understanding the Filler Effect on the Nucleation and Growth of C-S-H 3773, pp. 3764–3773. https://doi.org/10.1111/jace.13177.
BS EN 196-1:2016, 2016. British standard methods of testing cement - BS EN 196-1:2016. Determination of strength. Standard.
BS EN 197-1:2011. Composition, specifications and conformity criteria for common cements. Standard, 2011. November.
Cerveny, S., Arrese-Igor, S., Dolado, J.S., Gaitero, J.J., Alegria, A., Colmenero, J., 2011. Effect of hydration on the dielectric properties of C-S-H gel. J. Chem. Phys. 134 (3), 034509 https://doi.org/10.1063/1.3521481.
Chari, M.N., Shekarchi, M., Sobhani, J., Chari, M.N., 2016. The effect of temperature on the moisture transfer coefficient of cement-based mortars: an experimental investigation. Construct. Build. Mater. 102, 306–317. https://doi.org/10.1016/j.conbuildmat.2015.10.065.
Cuenca, E., Ferrara, L., 2017. Self-healing capacity of fiber reinforced cementitious composites. State of the art and perspectives. KSCE J. Civ. Eng. 21 (7), 2777–2789. https://doi.org/10.1007/s12205-017-0939-5.
E. Cuenca, A. Tejedor, L. Ferrara, A methodology to assess crack-sealing effectiveness of crystalline admixtures under repeated cracking-healing cycles, Construct. Build. Mater. 179. doi:10.1016/j.conbuildmat.2018.05.261.
T. Danner, U. H. Jakobsen, M. R. Geiker, Mineralogical sequence of self-healing products in cracked marine concrete, Minerals 9 (5). doi:10.3390/min9050284.
De Belie, N., Gruyaert, E., Al-Tabbaa, A., Antonaci, P., Baera, C., Bajare, D., Darquennes, A., Davies, R., Ferrara, L., Jefferson, T., Litina, C., Miljevic, B., Otlewska, A., Ranogajec, J., Roig-Flores, M., Paine, K., Lukowski, P., Serna, P., Tulliani, J.-M., Vucetic, S., Wang, J., Jonkers, H.M., 2018. A review of self-healing concrete for damage management of structures. Adv. Mater. Interfaces 5 (17), 1800074. https://doi.org/10.1002/admi.201800074.
C. De Nardi, D. Gardner, A. D. Jefferson, Development of 3D printed networks in self-healing concrete, Materials 13 (6). doi:10.3390/ma13061328.
Espinosa-Marzal, R.M., Hamilton, A., McNall, M., Whitaker, K., Scherer, G.W., 2011. The chemomechanics of crystallization during rewetting of limestone impregnated with sodium sulfate. J. Mater. Res. 26 (12), 1472–1481. https://doi.org/10.1557/jmr.2011.137.
Faber, J., Fawcett, T., 2002. The powder diffraction file: present and future. Acta Crystallogr. Sect. B Struct. Sci. 58 (3 PART 1), 325–332. https://doi.org/10.1107/S0108768102003312.
Ferrara, L., Krelani, V., Moretti, F., Roig Flores, M., Serna Ros, P., 2017. Effects of autogenous healing on the recovery of mechanical performance of high performance fibre reinforced cementitious composites (HPFRCCs): Part 1. Cement Concr. Compos. 83, 76–100. https://doi.org/10.1016/J.CEMCONCOMP.2017.07.010.
Ferrara, L., Mullem, T.V., Cruz, M., Antonaci, P., Paul, R., Cuenca, E., Jefferson, A., Ng, P.-l., Peled, A., Roig-flores, M., Sanchez, M., Schroefl, C., Serna, P., Snoeck, D., Marc, J., Belie, N.D., 2018. Experimental characterization of the self-healing capacity of cement based materials and its effects on the material performance: a state of the art report by COST Action SARCOS WG2. Construct. Build. Mater. 167, 115–142. https://doi.org/10.1016/j.conbuildmat.2018.01.143.
Gallé, C., 2001. Effect of drying on cement-based materials pore structure as identified by mercury intrusion porosimetry. Cement Concr. Res. 31 (10), 1467–1477. https://doi.org/10.1016/S0008-8846(01)00594-4.
D. Gardner, R. Lark, T. Jefferson, R. Davies, A survey on problems encountered in current concrete construction and the potential benefits of self-healing cementitious materials, Case Stud. Constr. Mater. 8. doi:10.1016/j.cscm.2018.02.002.
Gardner, D., Herbert, D., Jayaprakash, M., Jefferson, A., Paul, A., 2017. Capillary flow characteristics of an autogenic and autonomic healing agent for self-healing concrete. J. Mater. Civ. Eng. 29 (11), 04017228 https://doi.org/10.1061/(ASCE)MT.1943-5533.0002092.
Gopalan, M.K., 1996. Sorptivity of fly ash concretes. Cement Concr. Res. 26 (8), 1189–1197. https://doi.org/10.1016/0008-8846(96)00105-6.
Habert, G., Roussel, N., 2009. Study of two concrete mix-design strategies to reach carbon mitigation objectives. Cement Concr. Compos. 31 (6), 397–402. https://doi.org/10.1016/j.cemconcomp.2009.04.001.
Hall, C., Hall, C., 1989. Water sorptivity of mortars and concretes: a review. Mag. Concr. Res. 41 (147), 51–61. https://doi.org/10.1680/macr.1989.41.147.51.
Hall, C., Hamilton, A., 2018. Beyond the sorptivity: definition, measurement, and properties of the secondary sorptivity. J. Mater. Civ. Eng. 30 (4), 04018049 https://doi.org/10.1061/(ASCE)MT.1943-5533.0002226.
Hatungimana, D., Taskopru, C., Ichedef, M., Sac, M.M., Yazici, S., 2019. Compressive strength, water absorption, water sorptivity and surface radon exhalation rate of silica fume and fly ash based mortar. J. Build. Eng. 23, 369–376. https://doi.org/10.1016/J.JOBE.2019.01.011.
Huang, H., Ye, G., Qian, C., Schlangen, E., 2016. Self-healing in cementitious materials: materials, methods and service conditions. Mater. Des. 92, 499–511. https://doi.org/10.1016/j.matdes.2015.12.091.
Johannesson, B., Utgenannt, P., 2001. Microstructural changes caused by carbonation of cement mortar. Cement Concr. Res. 31 (6), 925–931. https://doi.org/10.1016/S0008-8846(01)00498-7.
Kajaste, R., Hurme, M., 2016. Cement industry greenhouse gas emissions - management options and abatement cost. J. Clean. Prod. 112, 4041–4052. https://doi.org/10.1016/j.jclepro.2015.07.055.
Kim, T., Tae, S., Roh, S., 2013. Assessment of the CO2 emission and cost reduction performance of a low-carbon-emission concrete mix design using an optimal mix design system. Renew. Sustain. Energy Rev. 25, 729–741. https://doi.org/10.1016/J.RSER.2013.05.013.
Koniorczyk, M., Konca, P., Gawin, D., 2013. Salt crystallization-induced damage of cement mortar microstructure investigated by multi-cycle mercury intrusion. In: VIII International Conference on Fracture Mechanics of Concrete and Concrete Structures FraMCoS-, vol. 8.
Leung, H., Kim, J., Nadeem, A., Jaganathan, J., Anwar, M., 2016. Sorptivity of self-compacting concrete containing fly ash and silica fume. Construct. Build. Mater. 113, 369–375. https://doi.org/10.1016/j.conbuildmat.2016.03.071.
Li, Z., de Souza, L.R., Litina, C., Markaki, A.E., Al-Tabbaa, A., 2020. A novel biomimetic design of a 3D vascular structure for self-healing in cementitious materials using Murray's law. Mater. Des. 190, 108572. https://doi.org/10.1016/j.matdes.2020.108572.
Liu, H., Zhang, Q., Gu, C., Su, H., Li, V., 2017. Influence of microcrack self-healing behavior on the permeability of Engineered Cementitious Composites. Cement Concr. Compos. 82, 14–22. https://doi.org/10.1016/J.CEMCONCOMP.2017.04.004.
Liu, S., Han, W., Li, Q., 2017. Hydration properties of ground granulated blast-furnace slag (GGBS) under different hydration environments. Mater. Sci. 23 (1), 70–77. https://doi.org/10.5755/j01.ms.23.1.14934.
Lothenbach, B., Scrivener, K., Hooton, R., 2011. Supplementary cementitious materials. Cement Concr. Res. 41 (12), 1244–1256. https://doi.org/10.1016/j.cemconres.2010.12.001.
Lothenbach, B., Durdzinski, P., de Weerdt, K., 2015. Thermogravimetric analysis. A Practical Guide to Microstructural Analysis of Cementitious Materials. CRC Press - Taylor & Francis group, pp. 177–211. Ch. 5.
Maddalena, R., Roberts, J.J., Hamilton, A., 2018. Can Portland cement be replaced by low-carbon alternative materials? A study on thermal properties and carbon emissions of innovative cements. J. Clean. Prod. 186, 933–942. https://doi.org/10.1016/j.jclepro.2018.02.138.
Maddalena, R., Hall, C., Hamilton, A., 2019. Effect of silica particle size on the formation of calcium silicate hydrate (C-S-H) using thermal analysis. Thermochim. Acta 672 (August 2018), 142–149. https://doi.org/10.1016/j.tca.2018.09.003.
Maddalena, R., Bonanno, L., Balzano, B., Sweeney, J., Mihai, I., 2020. A crack closure system for cementitious composite materials using knotted shape memory polymer (k-SMP) fibres. Cement Concr. Compos. 114 (May), 103757. https://doi.org/10.1016/j.cemconcomp.2020.103757.
Mehta, P.K., Monteiro, P.J., 2006. Concrete Microstructure, Properties and Materials, third ed. MCGraw-Hill.
Monteagudo, S.M., Moragues, A., Gálvez, J.C., Casati, M.J., Reyes, E., 2014. The degree of hydration assessment of blended cement pastes by differential thermal and thermogravimetric analysis. Morphological evolution of the solid phases. Thermochim. Acta 592, 37–51. https://doi.org/10.1016/j.tca.2014.08.008.
Mora, E., González, G., Romero, P., Castellón, E., 2019. Control of water absorption in concrete materials by modification with hybrid hydrophobic silica particles. Construct. Build. Mater. 221, 210–218. https://doi.org/10.1016/j.conbuildmat.2019.06.086.
Nishiwaki, T., Kwon, S., Homma, D., Yamada, M., Mihashi, H., 2014. Self-healing capability of fiber-reinforced cementitious composites for recovery of watertightness and mechanical properties. Materials 7, 2141–2154. https://doi.org/10.3390/ma7032141.
Park, B., Choi, Y.C., 2018. Quantitative evaluation of crack self-healing in cement-based materials by absorption test. Construct. Build. Mater. 184 https://doi.org/10.1016/j.conbuildmat.2018.06.206.
Park, B., Choi, Y.C., 2019. Prediction of Self-Healing Potential of Cementitious Materials Incorporating Crystalline Admixture by Isothermal Calorimetry. Int. J. Concr. Struct. Mater. 13 (1) https://doi.org/10.1186/s40069-019-0349-9.
Quercia, G., Spiesz, P., Husken, G., Brouwers, J., 2012. Effects of amorphous nano-silica addition on mechanical and durability performance of SCC mixtures. In: International Congress on Durability of Concrete.
M. Rajczakowska, L. Nilsson, K. Habermehl-Cwirzen, H. Hedlund, A. Cwirzen, Does a high amount of unhydrated Portland cement ensure an effective autogenous self-healing of mortar?, Materials 12 (20). doi:10.3390/ma12203298.
Ren, F., Zhou, C., Zeng, Q., Ding, Z., Xing, F., Wang, W., 2019. The dependence of capillary sorptivity and gas permeability on initial water content for unsaturated cement mortars. Cement Concr. Compos. 104 (February), 103356. https://doi.org/10.1016/j.cemconcomp.2019.103356.
Roels, S., Carmeliet, J., Hens, H., Adan, O., Brocken, H., Cerny, R., Pavlik, Z., Hall, C., Kumaran, K., Pel, L., Plagge, R., 2004. Interlaboratory comparison of hygric properties of porous building materials. J. Therm. Envelope Build. Sci. 27, 307–325. https://doi.org/10.1177/1097196304042119.
Saha, A.K., 2018. Effect of class F fly ash on the durability properties of concrete. Sustain. Environ. Res. 28 (1), 25–31. https://doi.org/10.1016/j.serj.2017.09.001.
Sahmaran, M., Yildirim, G., Erdem, T.K., 2013. Self-healing capability of cementitious composites incorporating different supplementary cementitious materials. Cement Concr. Compos. 35 (1), 89–101. https://doi.org/10.1016/j.cemconcomp.2012.08.013.
S. Sakir, S. N. Raman, M. Safiuddin, A. B. Amrul Kaish, A. A. Mutalib, Utilization of by-products and wastes as supplementary cementitious materials in structural mortar for sustainable construction, Sustainability 12 (9). doi:10.3390/su12093888.
Salas, D.A., Ramirez, A.D., Rodríguez, C.R., Petroche, D.M., Boero, A.J., Duque-Rivera, J., 2016. Environmental impacts, life cycle assessment and potential improvement measures for cement production: a literature review. J. Clean. Prod. 113, 114–122. https://doi.org/10.1016/j.jclepro.2015.11.078.
Sidiq, A., Gravina, R.J., Setunge, S., Giustozzi, F., 2020. High-efficiency techniques and micro-structural parameters to evaluate concrete self-healing using X-ray tomography and Mercury Intrusion Porosimetry: a review. Construct. Build. Mater. 252, 119030. https://doi.org/10.1016/j.conbuildmat.2020.119030.
Snoeck, D., De Belie, N., 2016. Repeated autogenous healing in strain-hardening cementitious composites by using superabsorbent polymers. J. Mater. Civ. Eng. 28 (1), 04015086 https://doi.org/10.1061/(ASCE)MT.1943-5533.0001360.

D. Snoeck, J. Dewanckele, V. Cnudde, N. De Belie, X-ray computed microtomography to study autogenous healing of cementitious materials promoted by superabsorbent polymers, Cement Concr. Compos. 65. doi:10.1016/j.cemconcomp.2015.10.016.

Tan, L., Reeksting, B., Ferrandiz-Mas, V., Heath, A., Gebhard, S., Paine, K., 2020. Effect of carbonation on bacteria-based self-healing of cementitious composites. Construct. Build. Mater. 257, 119501. https://doi.org/10.1016/j.conbuildmat.2020.119501.

Teall, O., Pilegis, M., Davies, R., Sweeney, J., Jefferson, T., Lark, R., Gardner, D., 2018. A shape memory polymer concrete crack closure system activated by electrical current. Smart Mater. Struct. 27 (7), 075016 https://doi.org/10.1088/1361-665X/aac28a.

Treacy, M., Meng, N., Paciacconi, A., 2019. What added value can SHM bring to my construction project or structure maintenance programme?. In: SMAR2019 - Fifth Conference on Smart Monitoring. Assessment and Rehabilitation of Civil Structures, pp. 1–8.

E. Tziviloglou, V. Wiktor, H. M. Jonkers, E. Schlangen, Bacteria-based self-healing concrete to increase liquid tightness of cracks, Construct. Build. Mater. 122. doi: 10.1016/j.conbuildmat.2016.06.080.

United Nations, 2019. The Sustainable Development Goals Report 2019. Tech. rep., United Nations, New York, NY. https://undocs.org/E/2019/68.

Van Mullem, T., Anglani, G., Dudek, M., Vanoutrive, H., Bumanis, G., Litina, C., Kwiecień, A., Al-Tabbaa, A., Bajare, D., Stryszewska, T., Caspeele, R., Van Tittelboom, K., Jean-Marc, T., Gruyaert, E., Antonaci, P., De Belie, N., 2020. Addressing the need for standardization of test methods for self-healing concrete: an inter-laboratory study on concrete with macrocapsules. Sci. Technol. Adv. Mater. 21 (1), 661–682. https://doi.org/10.1080/14686996.2020.1814117.

Van Tittelboom, K., Gruyaert, E., Rahier, H., De Belie, N., 2012. Influence of mix composition on the extent of autogenous crack healing by continued hydration or calcium carbonate formation. Construct. Build. Mater. 37, 349–359. https://doi.org/10.1016/j.conbuildmat.2012.07.026.

Villagrán Zaccardi, Y.A., Alderete, N.M., De Belie, N., 2017. Improved model for capillary absorption in cementitious materials: progress over the fourth root of time. Cement Concr. Res. 100, 153–165. https://doi.org/10.1016/J.CEMCONRES.2017.07.003.

Wainwright, P.J., Rey, N., 2000. The influence of ground granulated blastfurnace slag (GGBS) additions and time delay on the bleeding of concrete. Cement Concr. Compos. 22, 253–257. https://doi.org/10.1017/CBO9781107415324.004.

Wang, J.Y., Soens, H., Verstraete, W., De Belie, N., 2014. Self-healing concrete by use of microencapsulated bacterial spores. Cement Concr. Res. 56, 139–152. https://doi.org/10.1016/j.cemconres.2013.11.009.

Wang, X.F., Yang, Z.H., Fang, C., Han, N.X., Zhu, G.M., Tang, J.N., Xing, F., 2019. Evaluation of the mechanical performance recovery of self-healing cementitious materials – its methods and future development: a review. Construct. Build. Mater. 212, 400–421. https://doi.org/10.1016/j.conbuildmat.2019.03.117.

Yildirim, G., Khiavi, A.H., Yesilmen, S., Sahmaran, M., 2018. Self-healing performance of aged cementitious composites. Cement Concr. Compos. 87, 172–186. https://doi.org/10.1016/j.cemconcomp.2018.01.004.

Zhang, Z., Qian, S., Ma, H., 2014. Investigating mechanical properties and self-healing behavior of micro-cracked ECC with different volume of fly ash. Construct. Build. Mater. 52, 17–23. https://doi.org/10.1016/j.conbuildmat.2013.11.001.

Zhang, Y., Yang, B., Yang, Z., Ye, G., 2019. Ink-bottle effect and pore size distribution of cementitious materials identified by pressurization – depressurization cycling mercury. Materials 12 (1454), 1–15. https://doi.org/10.3390/ma12091454.